

1 **Environmental Conditions Associated with Observed Snowband Structures**
2 **within Northeast U.S. Winter Storms**

3
4 Sara A. Ganetis^{1,3}, Brian A. Colle¹, Sandra E. Yuter² and Nicole P. Hoban²

5 ¹*School of Marine and Atmospheric Sciences, Stony Brook University / SUNY,*

6 *Stony Brook, New York*

7 ²*Department of Marine, Earth, and Atmospheric Sciences, North Carolina State University,*

8 *Raleigh, North Carolina*

9 ³*I.M. Systems Group, Inc., and Weather Prediction Center, NOAA/NWS/NCEP, College Park,*

10 *Maryland*

11
12 For submission to *Monthly Weather Review*

13 12 February 2017

14
15
16
17
18
19
20
21
22
23
24 *Corresponding author address:* Brian A. Colle, School of Marine and Atmospheric Sciences, Stony
25 Brook University / SUNY, Stony Brook, NY 11794-5000.
26 Email: brian.colle@stonybrook.edu

27 **Abstract**

28 Northeast U.S. winter storms commonly exhibit multiple meso- β scale ($L < 200$ km)
29 bands of enhanced radar reflectivity and precipitation. We use radar observations, upper air
30 soundings, and reanalyses from 108 cases of cool-season (Oct-Apr) storms from 1996-2016 that
31 occurred within the coastal corridor from Delaware to Maine. Banding can occur in several
32 configurations among storms, and banding characteristics can differ at different times within the
33 same storm. We classified 6-hour storm periods as containing long (> 200 km) single bands,
34 single bands co-occurring with sets of mesoscale multi-bands, multi-bands only, and radar echo
35 without any bands using a combination of automated and manual methods. Use of radar
36 reflectivity data at 0.5 dB precision and criteria that identified local enhancements as bands
37 rather than a fixed threshold showed that the occurrence of long single bands without any
38 mesoscale multi-bands was rare. The most frequently occurring band configuration (55%) was
39 co-occurring single bands and multi-bands, which usually occurred in the northwest quadrant of
40 mature cyclones. Sets of multi-bands without a nearby single band usually occurred in the
41 northeast quadrant of a cyclone poleward of weak-midlevel forcing along a warm front. Overall,
42 mesoscale multi-bands more commonly occurred after the cyclone occluded than in the
43 developing stages. Multi-bands occurred in a wide range of frontogenesis and moist potential
44 vorticity environments.

47 **1. Introduction**

48 Mesoscale banding within United States (U.S.) East Coast winter storms can lead to
49 localized heavy snowfall rates and accumulations that can negatively impact lives and property
50 within the heavily populated urban corridors of the Mid-Atlantic and New England states. For
51 example, the recent blizzard of 8–9 February 2013 exhibited an intense mesoscale snowband and
52 resulted in power outages impacting 600,000 homes, over 6,000 cancelled flights, and 18
53 fatalities (Krekeler 2013; Picca et al. 2014; Ganetis and Colle 2015). Winter storms exhibit bands
54 with a variety of sizes, motions, and intensities (Novak et al. 2004; Kenyon 2013), but most
55 studies have investigated the primary band, or a single snowband with length (L) $>$ 200 km. In
56 these previous studies, the use of radar data and mosaics based on Level III radar reflectivities
57 with 5 dB steps made it difficult to discern the groups of smaller, multiple bands with $L <$ 200
58 km that also impact snowfall accumulation. For example, the 26–27 December 2010 East Coast
59 winter storm produced over 10 finescale (5–20-km wide and 10–100-km long) bands that led to
60 over 6,000 cancelled flights and regional train service (Soltow 2011; Kocin et al. 2011). A
61 detailed analysis and comparison of the multi-band environment with that of the single band
62 within winter storms is needed to enhance understanding and prediction of these bands.

63 Mesoscale bands found within the comma head of developing and mature extratropical
64 cyclones impacting the U.S. East Coast have been studied using conventional radar data for
65 classification (e.g., Novak et al. 2004; 2010; Kenyon et al. 2013). The primary band, hereafter
66 referred to as a single snowband with $L >$ 200 km, is typically found to the northwest of a surface
67 low pressure center and coincides with the ascending branch of the ageostrophic frontogenetical
68 circulation. This ascent and associated single band is narrowed and enhanced on the warm side
69 of a mid-level frontal boundary in an environment with conditional symmetric instability (CSI)

70 or weak moist symmetric stability (Emanuel 1985; Thorpe and Emanuel 1985; Xu 1989).
71 Although single snowbands are usually the focus of many winter mesoscale precipitation studies
72 (e.g. Sanders and Bosart 1985a,b; Wolfsberg et al. 1986; Novak et al. 2004, 2008, 2009, 2010,
73 2012; Moore et al. 2005; Picca et al. 2014; Colle et al. 2014; Baxter and Schumacher 2017)
74 smaller multi-bands, or multiple parallel bands with $L < 200$ km, are found embedded within the
75 comma head region of an extratropical cyclone and are less understood. One reason most studies
76 did not investigate multi-bands was the lack of access to fine scale observations or gridded
77 reanalysis data (Novak 2009).

78 Although comparisons of case studies of banding within individual winter storms are
79 prevalent in the literature (e.g. Nicosia and Grumm 1999; Jurewicz and Evans 2004), multiyear
80 climatological studies consisting of > 5 storms are less numerous. Novak et al. (2004) used
81 mosaic radar reflectivity data to identify 88 cases from 1996 to 2001. Their study employed a
82 subjective classification scheme of the reflectivity data that included single bands, narrow cold-
83 frontal rainbands, and multi-bands. They compared the environments between single bands and
84 non-banded cases. The climatological study by Novak et al. (2010) aimed to isolate the role of
85 moist processes in the evolution of the single-banded environment. Using the methodology from
86 Novak et al. (2004), they identified 144 heavy precipitation cases from 2002 to 2008, out of the
87 75 that exhibited a closed 700-hPa low, 30 single-banded cases were examined. Novak et al.
88 (2010) utilized single, transitory and null categories in the classification scheme with no
89 separation of multi-bands. The main results of their study were that mid-level frontogenesis was
90 stronger for banded events than null events and CI was more prevalent than CSI during single
91 band formation. The lifecycle of single bands was examined in the context of frontogenetical
92 ascent within a layer of CI. Bands dissipated when upstream diabatic PV anomalies and

93 geopotential height falls shifted the location of maximum frontogenetical forcing away from the
94 existing primary band.

95 Most band classification studies have relied on the human eye for band identification and
96 classification (e.g., Novak et al. 2004; 2010; Kenyon et al. 2013). The first automated CONUS-
97 wide study of banded precipitation was created by Fairman et al. (2016). Using image processing
98 methods on composite radar imagery, they found that for Dec–Feb from 2003–2014 the
99 Northeast U.S. experiences relative peaks in the banded precipitation in the Tug Hill Plateau of
100 upstate NY and lee of Lake Erie in western NY (likely associated with lake-effect precipitation
101 bands) and within the Ohio Valley extending across the Appalachians to the coast of NJ (likely
102 associated with banding within extratropical cyclones). This was a large-scale study focusing on
103 banded features with a major axis ≥ 100 km, therefore smaller-scale bands, especially those
104 embedded within the comma head of extratropical cyclones, were not addressed.

105 Climatological studies of bands have been conducted for storms impacting the West
106 Coast and East Coast of the United States, but questions remain with how banding within
107 continental cyclones compared. A recent climatology of single-banded snowfall in Central U.S.
108 cyclones (between the Rocky and Appalachian Mountains) was conducted by Baxter and
109 Schumacher (2017) using 1-km composite radar imagery for 66 cyclones exhibiting ≥ 4 in (10.16
110 cm) of accumulated snowfall during 5 cool seasons from 2006–2011. Their study manually
111 identified single bands that were ≥ 250 km long and defined events every 3 hours within a storm.
112 Out of the 66 cyclones, there were 98 banded events and 38 non-banded events. The average
113 snowband lasted 5.2 h, was 45 km wide and 428 km long. Out of the banded events, 54 occurred
114 in the northeast (NE) quadrant relative to the cyclone center, 29 in the northwest (NW) quadrant,
115 and 15 within both northern quadrants. Out of the 38 non-banded events, the precipitation

116 coverage occurred in both northern quadrants for 28 events. Their study differed from that of the
117 East Coast winter storm analysis of Novak et al. (2004) in that this study found nearly twice as
118 many non-banded events and more single bands formed in the NE rather than the NW quadrant.

119 Our paper aims to answer the following fundamental questions regarding single and
120 multi-bands in the comma head region of extratropical cyclones in the Northeast U.S.:

- 121 • What is the distribution of single bands, multi-bands, and non-banded events identified
122 using quasi-objective methods?
- 123 • How do vertical profiles of available moisture, instability, lift and wind shear differ
124 among multi-bands and single bands as well non-banded precipitation areas in the comma
125 head?

126 One goal of this research is to create a multi-year dataset consisting of cool season
127 (October through April) precipitation events that are identified and classified using
128 predominately objective methods. This dataset can be compared with that of previous
129 climatological studies that relied on manual classification methods. A potential caveat of using a
130 solely objective method is that various fields, specifically radar reflectivity, can contain a wide
131 range of values during one time in a single storm. The method can be tuned to produce minimal
132 error when compared with subjective methods for one single storm, but may fail when applied to
133 a different storm. The objective methodology applied to the data in this study is discussed,
134 including the many tests that were conducted. Ultimately, subjective methods were also
135 employed for the final banding classification steps in this work in order to implement consistent
136 classification among diverse storms.

137 This paper is organized as follows: Section 2 describes the methods used to identify and
138 classify precipitation bands in Northeast U.S. winter storms. Section 3 explores the cyclone-

139 relative band classification. Section 4 discusses the thermodynamic environment of the various
140 classifications of precipitation bands with a focus on contrasting known banding environmental
141 ingredients (i.e., moisture, instability, lift). Finally, section 5 summarizes the main results of this
142 banding study.

143

144 **2. Data and Methods**

145 *a. Case identification*

146 Cases were identified as cool season (October - April) low pressure systems that tracked
147 through the Northeast U.S. between 1996/97 - 2015/16 with ≥ 1.00 in (2.54 cm) of liquid
148 equivalent snowfall measured at ≥ 2 of 7 Automated Surface Observing System (ASOS) stations
149 across the northeast United States (Fig. 1), which consisted of Portland, ME, Islip, NY, Boston,
150 MA, Philadelphia, PA, Bridgeport, CT, Providence, RI, and Newark, NJ (Hoban 2016). Over
151 150 cases were initially identified using this metric over 20 cool seasons, but 108 were ultimately
152 used based on radar data availability from six coastal radars (Fig. 1). Each case could span
153 multiple days, depending on the speed and extent of the affecting cyclone, but such days were
154 consolidated into a single case within the database. This resulted in a total of 108 unique cases.

155

156 *b. Cyclone tracking*

157 The band location relative to the parent surface cyclone center (i.e., nearest sea level
158 pressure minimum) is used in this study to provide a storm relative framework and to compare
159 with recent studies that highlight single bands form in the northwest quadrant for NEUS storms
160 (Novak et al. 2004) or the northeast quadrant for continental U.S. storms (Baxter and
161 Schumacher 2017). The sea-level pressure data for the cyclone tracks were obtained from the
162 from the 6 hourly 0.5° NCEP Climate Forecast System Reanalysis (CFSR; Saha et. al. 2010) for

163 years it is available (1996–2010) and then from the 6 hourly 0.5° NCEP Climate Forecast
164 System version 2 (CFSv2; Saha et al. 2014) analyses (2011–2016). Other reanalysis data were
165 considered, especially the North American Regional Reanalysis (NARR). Charles and Colle
166 (2009) showed that the NARR had a weak sea level pressure bias for cyclones along the U.S.
167 East Coast that was not shown with the CFSR (Colle et al. 2013). Thus, the CFSR was used in
168 favor of the NARR.

169 In order to track the extratropical cyclones on a common grid, the Hodges (1995) cyclone
170 tracking scheme was implemented according to the methodology provided in Colle et al. (2013).
171 Only those storms are tracked that last at least 24 hours and move farther than 1000 km. The
172 minimum lifetime and minimum moving distance are set to remove the features that are too
173 short-lived or remain too stationary. If there were multiple cyclones in the NEUS domain for a
174 particular case, the cyclone subjectively determined to be more associated with the observed
175 precipitation as shown by the radar reflectivity regional composite discussed in section 2c was
176 manually selected. If a cyclone track did not appear for a particular case because the cyclone was
177 too weak to be identified then the NOAA Weather Prediction Center (WPC) surface analyses for
178 that date and time were used to subjectively track the manually-identified low pressure center
179 every 6-h. The cyclone tracks for each case used in this study are shown in Figure 2.

180

181 *c. Regional composite radar dataset*

182 The radar data processing methods are described in detail in Hoban (2016) and Corbin
183 (2016) and are summarized in this section. Level II data from each of the six radars (KGYX,
184 KENX, KBOX, KOKX, KDIX, KDOX in Figure 1) were downloaded from the National Center
185 for Environmental Information (NCEI) radar archive and quality controlled to remove non-
186 meteorological echo within individual elevation angles in polar coordinates. Analysis of

187 overlapping echo regions at equal distances between adjacent radars were used to apply a relative
188 radar reflectivity calibration with respect to KOKX observed values. The polar coordinate data
189 were then interpolated to a 2 km x 2 km Cartesian grid at a constant elevation of 2 km AGL
190 extending 200 km radius from each site for every 6-10 min during each storm. For the duration
191 of each storm, regional maps of radar reflectivity were constructed by regridding each volume
192 scan to a common 801 km x 801 km grid with 2 km horizontal grid spacing. Since the timing of
193 volume scans among radars were not synchronized, KOKX was used as the central reference
194 radar and data from other 5 radars were used as long as their volume start time was within 8 min
195 of the volume start time at KOKX. There are sometimes gaps in the regional maps when data
196 from an individual radar was not available in the NCEI archive. This analysis uses 5-minute
197 Level II radar reflectivity data (0.5 dB precision) for every volume scan \pm 1 h from a 6-hourly
198 analysis time during the storm. An important distinction between this study and previous studies
199 such as Novak et al. (2004) and Kenyon (2013) is that they used Level III radar reflectivity data
200 (5 dB precision).

201

202 *d. Objective identification of bands*

203 Precipitation bands are classified from automatically-detected objects from the gridded
204 reflectivity data. The Method for Object-Based Diagnostic Evaluation (MODE) tool within the
205 Model Evaluation Tools (MET) version 5.1 developed at the Developmental Testbed Center
206 (DTC) at the Research Applications Laboratory (RAL) at the National Center for Atmospheric
207 Research (NCAR) was used to objectively identify precipitation structures in the stitched
208 regional composite radar data (Developmental Testbed Center 2015; Davis 2006a,b; Brown et al.
209 2007; Bullock et al. 2016).

210 Masking using an adaptive threshold was used to identify candidate objects with locally

211 enhanced radar reflectivity which were then filtered based on geometric attributes to classify
212 large bands, midsized bands, and undefined enhanced reflectivity regions. Masking was used to
213 create a binary field that equals 1 above the threshold and 0 elsewhere. The adaptive threshold
214 value for the reflectivity field varies during each case. Lawson and Gallus (2016) found that
215 objective identification and verification of reflectivity data using a similar method exhibited
216 substantial sensitivity to the reflectivity threshold chosen for summertime convection. They
217 found that using too low of a reflectivity value (5 dBZ) yielded too small of a sample size of
218 objects, but using too high of a value (40 dBZ) lost other features, i.e., stratiform precipitation.
219 They concluded that the threshold chosen should be done so to focus on the signal of interest. In
220 a study of banding throughout all four seasons, Fairman et al. (2016) chose a static threshold
221 value of 20 dBZ.

222 In this study, the adaptive threshold for each case results from a series of tests on 10
223 example cases. Bulk statistics were computed from the regional composite reflectivity data for
224 both the entire storm duration and for individual times during the storm. The following quantities
225 were calculated: minimum, lower-dectile, lower-octile, lower-quartile, median, mean, upper-
226 quartile, upper-octile, upper-dectile, and maximum. Data were used throughout the entire
227 regional radar composite domain and also tested on a sub-region centered over Long Island, NY.

228 The adaptive threshold that was found to work best through manual verification of 10
229 cases was the upper-sextile of the reflectivity throughout the Northeast U.S. domain at *each* time
230 within a storm. That meant that 17% of the reflectivity data is at or above this value, therefore
231 highlighting the enhancements of snowbands within the weaker, smaller reflectivity values.
232 Many sensitivity tests were conducted for this thresholding method calculated over the entire
233 region. The upper-quartile was found to be too low and failed to separate individual bands of

234 higher reflectivity embedded within widespread precipitation. The upper-octile was found to be
235 too high of a threshold that trimmed bands down, therefore underestimating their spatial
236 characteristics. This upper-sextile threshold was used to create the masked field at each time
237 available during each case.

238 Once the masked field is computed, objects are identified with the MODE tool as regions
239 that are continuous in space. If there is even one grid point separating the objects, they are
240 identified as separate objects. Attributes are computed for each object and include the object area
241 which is the number of grid squares an object occupies and the centroid, or geometric center, of
242 an object. The length, width, aspect ratio, and axis angle are computed by fitting a rectangle
243 around each object. The aspect ratio is the ratio of the short axis to the long axis. The axis angle
244 is the angle of the long axis of the rectangle relative to 90° (east).

245 There is a large variation of storm (and reflectivity) intensity among all 108 storms that
246 ultimately motivated the time-varying adaptive threshold. However, this time-varying threshold
247 was not without its limitations. There were times when a weaker band existed during a stronger
248 storm with too high a reflectivity threshold that resulted in a failure of the method. The threshold
249 was often skewed higher by offshore rain in several storms when a portion of the storm was over
250 warm Gulf Stream waters. This method did not work well for 8 out of 108 storms during which
251 manual methods had to be employed to subjectively identify (i.e., use the human eye on the raw
252 observed reflectivity field) instead of relying on the objective methods.

253

254 *e. Classification of bands*

255 Classification was first completed by post-processing the data output from MODE.

256 Objects were determined to be snowbands if their aspect ratios (length of minor axis divided by

257 the length of major axis) was ≤ 0.5 . The bands were additionally classified into large bands, mid-
258 sized bands, or undefined according to the length and width criteria provided in Table 1.

259 Next, both the classified field and the raw reflectivity field were analyzed to subjectively
260 classify dominant banding types within one region of the storm at each 6-hourly analysis time
261 during a case (i.e., 0000, 0600, 1200, 1800 UTC). The classifications were one of four different
262 categories based on the types of objects that were identified ± 1 h of the analysis time within one
263 boxed sounding domain extending 150 km from each of the 6 sounding locations in Figure 1
264 (i.e., KGYX, KALB, KCHH, KOKX, KIAD, KWAL) every 6 h during a case. An event was
265 classified if the radar echo was found in $\geq 50\%$ of the sounding domain box for ≥ 2 h. The use of
266 6-hourly events is consistent with what had been done in previous studies (e.g., Novak et al.
267 2004; Baxter and Schumacher 2017). The four storm-band categories were adapted from Novak
268 et al. (2004, their Table 1). The first category is for a storm that exhibits a large band ($L \geq 200$
269 km) and no other identified structures in the sounding domain and is termed the single band
270 category (SINGLE). The second category is for a storm that exhibits ≥ 2 mid-sized bands that are
271 parallel to each other and move similarly in the sounding domain and is the multi-band category
272 (MULTI). The third category is for a storm that exhibits a large band accompanied by mid-sized
273 bands that exhibit similar motions and is termed the both single band and multi-bands category
274 (BOTH). The fourth and final category is for storms that exhibit none of the previous linear
275 precipitation structure classification criteria and is termed the non-banded category (NONE).
276 Figure 3 shows examples of cases in each of the four categories.

277

278 *f. Subjective classification of banding events for cyclone stage and movement*

279 There was a large amount of variability in the developmental stage of the cyclone
280 responsible for ≥ 1.0 in (2.54 cm) liquid equivalent snowfall in the study domain as well as band
281 motion manually observed within the storms of this study. This motivated the additional sub-
282 classification based on both cyclone stage and band motion (Table 2). Cyclone maturity has been
283 used in refining climatological studies such as by Novak et al. (2010) who used the presence of a
284 closed 700-hPa circulation to differentiate comma head cases (i.e., stronger cyclones that would
285 likely have precipitation wrapping around the center to form a comma head) from non-comma
286 head cases within their 6-year study. Kenyon et al. (2013) looked into band motion with a special
287 focus on both laterally translating and radially pivoting single bands.

288 Cyclone maturity during each 6-hour time was classified as either developing or mature
289 determined manually using the WPC surface analyses following the Norwegian and Shapiro and
290 Keyser cyclone models (Bjerknes and Solberg 1922; Shapiro and Keyser 1990; Colle et al.
291 2014). Specifically, developing storms were defined as having an open wave frontal structure
292 while mature cyclones were at the start of the occluded stage defined as when circulations
293 around a cyclone create an occluded front that separates the cold air behind the cold front from
294 the warm air ahead of the cold front (Schultz and Vaughan 2010). The location of the
295 precipitation band relative to the cyclone center can depend on cyclone maturity, such as forming
296 north of a warm front in a developing cyclone versus northwest along the occluded front in a
297 mature cyclone (Schultz and Vaughan 2010). The four storm-band categories were further
298 classified into developing and mature cyclones resulting in eight categories.

299 The 5-minute interval animations of reflectivity and classified bands were used to classify
300 geographic-centric band motion by animating ± 1 h on either side of the 6-hourly analysis time.
301 Band motion with respect to the long axis of the band was assessed. One or more bands were

302 classified as moving perpendicular or parallel to their long axis or axes. The perpendicular
303 classification is comparable to the laterally translating and pivoting classifications used by
304 Kenyon et al. (2013). The parallel classification is comparable to the laterally quasi-stationary
305 classification used by Kenyon et al. (2013). The results from their study showed that various
306 band motions resulted from different synoptic and mesoscale environments, so therefore were
307 taken into account within this study for comparison. The eight classifications of band type and
308 cyclone strength were further sub-classified into perpendicular and parallel moving bands,
309 resulting in 12 different classification categories. The non-banded (NONE) classification was
310 classified into developing or mature cyclones, but no motion criteria were applied because there
311 were no defined bands to base the classification on.

312

313 *g. Analysis of band environment*

314 Observed soundings from the six upper-air locations over the Northeast U.S. are available
315 approximately every 12 h (Fig. 1). To increase the temporal frequency of available vertical
316 profiles to every 6-h, vertical profiles were also derived at the nearest grid point to each observed
317 sounding location from the 0.5° resolution CFSR. This is the same analysis data used by Kenyon
318 et al. (2013) for their environmental band analysis. The Climate Forecast System version 2
319 (CFSv2; Saha et al. 2014), which was used for dates later than 2010, have data approximately
320 every 38 km horizontally with 64 vertical pressure levels (Saha et al. 2014). Our analysis focus is
321 above the boundary layer, thus minimizing the effect of terrain or surface type differences (e.g.
322 proximity to the coast at KOKX and KCHH).

323 The accuracy of these CFSR grid point profiles was determined by comparing 1292
324 available soundings every 6 h during each of the 108 events from the 6 coastal sites (Fig. 1). The
325 mean error of temperature was typically $\pm 2^{\circ}\text{C}$ and relative humidity $\pm 15\%$. The mean errors for

326 mixing ratio above the boundary layer (> 2 km AGL) are typically within ± 1 g kg⁻¹ and are
327 within ± 2 K for potential temperature. Based on this evaluation, the CFSR-derived soundings
328 were considered a reasonable estimate to the observed atmosphere and were subsequently used
329 for this study.

330 Each 6-h event corresponds to bands (or lack thereof) within a specific domain that is
331 centered on and extends ~ 150 km from a sounding site. Vertical profiles based on 6-h CSFR
332 reanalysis were taken at the sounding sites during each classified event. The 300 km x 300 km
333 domain size was chosen to minimize overlap between boxes while providing coverage across
334 most of the NEUS. The profile in the center of the domain provides information on the
335 environment and is cross-indexed with the band type, cyclone maturity, and band motion for that
336 particular time in that 300 km x 300 km box. We found that the same sort of bands occur over a
337 few hundred kilometer region, so we hypothesized that the center point within the box would be
338 reasonably representative of the region. We extracted additional vertical profiles from reanalysis
339 from other points in the box regions and found that for SINGLE and BOTH there was a larger
340 variation in the profile parameters than for MULTI and NONE. The original profiles in the
341 center of the box were determined to be a reasonable estimate of the environment because they
342 were comparable to the median value computed from the extra profiles.

343

344 **3. Cyclone-relative Band Classification**

345 *a. Distribution by event*

346 The results of the approximately 6-hourly event classifications produced a total of 193
347 events from the 108 cases. The distribution relative to the cyclone center is provided in Figure 4.
348 The initial classification into the four standard categories is as follows: 5 SINGLE, 35 MULTI,
349 107 BOTH, and 46 NONE. All 5 SINGLE events were associated with a mature cyclone and

350 most occurred in the northwest quadrant of a cyclone (Fig. 4a). MULTI events were
351 approximately equitably distributed between developing (18) and mature (17) cyclones. BOTH
352 events were less often observed with developing (43) than mature cyclones (64). NONE events
353 were more often associated with developing (29) than mature cyclones (17). The results of the
354 final application of the geographic-centric band movement classification are provided in Table 2.
355 While the distribution of counts of MULTI events was similar for both developing and mature
356 cyclones, the bands favored parallel movement when associated with developing cyclones versus
357 a perpendicular movement when associated with mature cyclones. For both mature and
358 developing cyclones, more multi-bands occurred in the northeast quadrant than the northwest
359 quadrant (Fig. 4b). A similar relationship for band motion is evident when comparing the motion
360 associated with BOTH events. Parallel band motion is favored when a cyclone is classified as
361 developing versus the perpendicular motion for when a cyclone is classified as mature.
362 Perpendicular band motion classified events typically occurred in the northwest quadrant of a
363 mature cyclone, while parallel band motion classified events typically occurred in the northeast
364 quadrant of a developing cyclone (Fig. 4c). Non-banded events were predominantly in the
365 eastern quadrants, favoring the northeast quadrant (Fig. 4d).

366 Figure 5 shows the band orientation in addition to the location relative to the cyclone
367 center for large bands from SINGLE and BOTH events for developing and mature cyclones.
368 There is a cluster in the northwest quadrant of bands oriented southwest-northeast which is
369 observed to match the orientation of enhanced baroclinic zones that will be analyzed in section 4.
370 More large bands in the northeast quadrant are associated with developing cyclones rather than
371 mature cyclones. The more west-east orientation of these large bands is thought to be due to their
372 collocation with the warm front. The band orientations and clustering in the northern quadrants is

373 consistent with similar analysis conducted by Novak et al. (2004) and Baxter and Schumacher
374 (2017).

375

376 **4. Vertical Profile Analysis**

377 Comparisons of the thermal, moisture, and kinematic variables from a representative
378 profile from 1000 hPa to 300 hPa from each event were examined. Significance is assessed via
379 bootstrapping (Wilks 2011); each classification dataset is resampled by replacing randomly
380 1,000 times. For all four datasets, the size for each resample is equivalent to the total number of
381 events in the original dataset (5 SINGLE, 35 MULTI, 107 BOTH, 46 NONE).

382 Given the common location within the comma head of a cyclone, there is little variation
383 in temperature and humidity profiles among the four classifications (Fig. 6). Multi-bands are
384 hypothesized to arise within a more conditionally unstable environment in which moist updrafts
385 can break down into several smaller circulations (Xu 1992). Individual profiles of saturation
386 equivalent potential temperature (θ_e^*) show the presence of weak conditional instability indicated
387 by a small decrease in θ_e^* with height for all classifications with 20% (7 profiles) of MULTI
388 exhibiting a 50-hPa deep conditionally unstable layer (≤ -0.02 K hPa⁻¹), the highest percentage
389 out of all classifications (Figs. 7a–e). The MULTI events have larger average wind shear (1000–
390 700 hPa) values, ~ 10.3 m s⁻¹ (20 kts) compared to the ~ 2.6 m s⁻¹ (5 kts) and ~ 5.1 m s⁻¹ (10 kts)
391 for SINGLE and BOTH, respectively (Fig. 7j). This suggests that multi-bands may be associated
392 with shear-induced waves traveling within a ducted stable layer which will be explored in a
393 future case study.

394 Larger, single bands are hypothesized to be associated with stronger forcing for lift via
395 frontogenesis than multi-bands, especially given their preferential location in the northwest
396 quadrant of low pressure systems. Multi-bands may exist in an environment of weaker forcing

397 for lift but greater instability yielding more intermittent pockets of rising air that are more
 398 spatially dispersed as compared to sustained and concentrated lift with single band in strong
 399 frontogenesis. To test this, average profiles of 2-D Petterssen (1936) frontogenesis (Eq. 1; as in
 400 Novak et al. 2004, their Eq. 1) were computed for SINGLE and BOTH events (Figs. 8a,c) and
 401 compared to MULTI (Fig. 8b).

$$402 \quad F_{2D} = \frac{1}{|\nabla\theta|} \left(-\frac{\partial\theta}{\partial x} \left(\frac{\partial u}{\partial x} \frac{\partial\theta}{\partial x} + \frac{\partial v}{\partial x} \frac{\partial\theta}{\partial y} \right) - \frac{\partial\theta}{\partial y} \left(\frac{\partial u}{\partial y} \frac{\partial\theta}{\partial x} + \frac{\partial v}{\partial y} \frac{\partial\theta}{\partial y} \right) \right) \quad \text{Eq. 1}$$

403 Equation 1 of frontogenesis (F_{2D}) includes the gradients in the zonal (x) and meridional (y)
 404 directions of potential temperature (θ), and the zonal and meridional components of the wind (u
 405 and v , respectively). Non-banded environments were associated with lower values of
 406 frontogenesis than other classifications (Fig. 8d). At 700-hPa, the mean value of frontogenesis
 407 for NONE is statistically different than the mean value for BOTH at the 95% confidence interval
 408 (Fig. 8e).

409 Conditional symmetric instability (CSI) is indicated by negative values of saturation
 410 equivalent potential vorticity (MPV*; Eqs. 2-3; McCann 1995) in the absence of inertial and
 411 conditional instability (Schultz and Schumacher 1999).

$$412 \quad MPV^* = \frac{1}{\rho} \eta \cdot \nabla\theta_e^* \quad \text{Eq. 2}$$

$$413 \quad MPV^* = g \left(\left(\frac{\partial\theta_e^*}{\partial x} \frac{\partial v}{\partial P} \right) - \left(\frac{\partial\theta_e^*}{\partial y} \frac{\partial u}{\partial P} \right) - \frac{\partial\theta_e^*}{\partial P} \left(\frac{\partial v}{\partial x} - \frac{\partial u}{\partial y} + f \right) \right), \quad \text{Eq. 3}$$

414 in which g is gravity, P is pressure, f is the Coriolis parameter equal to $2\Omega\sin\phi$ where ϕ is
 415 latitude, ρ is the density, η is the absolute vorticity vector and θ_e^* is the saturation equivalent
 416 potential temperature. Equation 3 follows from Equation 2 assuming the horizontal gradient of
 417 the vertical wind speed is small and can be neglected. Banded precipitation has been related to

418 CSI (negative MPV*) via the following components of the conceptual model put forth by Clark
419 et al. (2002): (1) a region of mid-troposphere frontogenesis over the banded precipitation region,
420 (2) a saturated mesoscale updraft on the warm side of the frontogenesis region, (3) negative
421 MPV production near the updraft dominated by differential vertical theta-e transport, and (4)
422 release of CSI leading to banded precipitation. Negative value of MPV* would indicate the
423 presence of CSI in the absence of CI, a known instability responsible for enhancing circulations
424 associated with some single bands (Novak et al. 2010). Average profiles of MPV* were
425 calculated from the 4 closest grid points centered on the sounding location for all levels. CSI is
426 evident in the average profiles of all classification types below 600 hPa (Figs. 8f–i). The most
427 negative values in the average profiles of MPV* are found between 900–800-hPa for all
428 classifications, with $MPV^* < 0$ and statistically insignificant differences among the
429 classifications between 700–550-hPa (Fig. 8j).

430 Looking at one particular level (e.g., 700 hPa), frontogenesis was calculated along with
431 the stability in the 100-hPa layer extending to 600-hPa and the layer-averaged value of MPV*
432 (Fig. 9). The NONE events exhibit the weakest frontogenesis ($< 2 \text{ K (100 km 1 h)}^{-1}$). BOTH
433 events had the largest frontogenetical values with 21 of 107 (~20%) events associated with
434 frontogenesis $> 1.5 \text{ K (100 km 1 h)}^{-1}$. No BOTH events exhibited 700–600-hPa conditionally
435 unstable layers (θ_e^* decreasing with height) but 99 of 107 (93%) events were associated with
436 moist symmetric instability ($MPV^* < 0$). One of the MULTI events exhibited conditional
437 instability but 34 events exhibited conditional symmetric instability. The MULTI environment
438 showed relatively weak frontogenesis values with 34 events $< 1.5 \text{ K (100 km 1 h)}^{-1}$. For MULTI
439 cases, frontogenesis is slightly larger at other levels (e.g., 850 hPa) but still smaller than that of

440 BOTH and SINGLE, which suggests an alternative forcing source other than frontogenesis
441 yields these bands.

442

443 **5. Summary and Discussion**

444 A combination of objective and subjective approaches for the classification of bands of
445 108 NEUS winter storms from 1996–2016 was conducted. The dataset was comprised of
446 extratropical cyclones that produced ≥ 1.00 in (2.54 cm) per day liquid equivalent snowfall at
447 least 2 of 7 ASOS stations along the eastern seaboard from Delaware to Maine. Regional
448 composite 2-km AGL radar reflectivity data from six coastal NEUS radars were used to identify
449 and classify bands using the Model Evaluation Tools (MET) Method for Object-based
450 Diagnostic Evaluation (MODE), specifically into large bands ($L \geq 200$ km) and mid-sized bands
451 ($L < 200$ km) both with aspect ratios (ratio of width to length) ≤ 0.5 . At each 6-hourly analysis
452 time, the portions of the storm falling within each of six 300 km x 300 km boxes centered on
453 operational sounding sites were categorized as containing either: a single band only (SINGLE),
454 multi-bands only (MULTI), both single and multi-bands (BOTH), or as non-banded (NONE) for
455 radar echoes present in $\geq 50\%$ of the box ≥ 2 h. This resulted in 193 classified storm sub-periods
456 from 108 storms with the most common categories being BOTH (107) and NONE (46), followed
457 by MULTI (35) and SINGLE (5) (Table 2). This study found that single bands unaccompanied
458 by multi-bands are actually quite rare compared to the findings of previous studies. This
459 discrepancy is likely a result of the 5-dBZ binning of the reflectivity field that others used,
460 compared to our analysis that used 0.5 dB precision Level 2 radar data and a method that
461 detected locally enhanced features relative to a changing background.

462 Additional information was used to further sub-classify the categories by their association

463 with a developing or mature cyclone and the type of geographic-centric band movement
464 exhibited as being either moving perpendicular to the long axis or moving parallel to the long
465 axis. Developing cyclones were predominantly associated with parallel moving bands (69%) that
466 were clustered in the northeast quadrant. Mature cyclones most often exhibited BOTH (48%) in
467 the northwest quadrant, MULTI (17%) in the northeast quadrant, NONE (17%) in the eastern
468 quadrants, and SINGLE (5%) in the northwest quadrant. Mature cyclones were predominantly
469 associated with perpendicular moving bands (87%) that occurred most frequently in the
470 northwest quadrant of the cyclone.

471 CFSR and CFSv2 analyses were used to compare environmental variables of the known
472 important single banding ingredients of lift, instability, and moisture for the different banding
473 classifications. A simple frontogenesis threshold does not distinguish among band categories
474 (Fig. 10). While single only and both single and multi-band occurred in environments of strong
475 frontogenesis, they also occurred with moderate and with weak frontogenesis. Multi-band and no
476 banding occurred in conditions of moderate to weak frontogenesis. The combination of MPV
477 and frontogenesis does not clearly distinguish among band categories either. Hence, while the
478 presence of strong frontogenesis increases the likelihood of a single band forming, these long
479 bands as well as shorter multi-bands do form in weaker forcing conditions. This suggests that
480 other lifting processes may be important and need to be explored, such as gravity waves or
481 vertical shear instabilities. MULTI cases exhibited larger 1000-700-hPa wind shear compared to
482 SINGLE and BOTH and the importance of this result will be explored in a future case study.

483 MULTI and BOTH typically exhibit a 200-hPa layer of conditional symmetric instability
484 (CSI indicated by $MPV^* < 0$ PVU) more often than conditional instability (CI). Previous studies
485 suggest that CSI is the dominant instability responsible for multiple bands from analysis of one

486 case or synoptic situation (e.g., Shields et al. 1991, Xu 1992) to three cases (Nicosia and Grumm
487 1999). However, Novak et al. (2010) found that CI occurred more often than CSI for dozens of
488 single band cases within mature cyclones. Furthermore, Schultz and Schumacher (1999) found
489 that CSI is not a guaranteed instability that is always associated with banding. CI might be
490 important for multi-bands within BOTH events but a relationship is not clear for MULTI events
491 which requires additional investigation. NONE events show shallow near-surface layers of CSI,
492 but even if the instability is present it might not be released without air being lifted via
493 frontogenesis and therefore results in a lack of banding. There was no significant difference in
494 the third banding ingredient, moisture, among the classifications likely due to the common
495 location in the near-saturated environment of the cyclone comma head. General differences
496 among banded environments are provided in this paper. Future work could utilize both
497 observations and a high-resolution mesoscale model to explore some of the mechanisms for
498 multi-band development as well as analyze the evolutions of single and multi-bands, separately,
499 to examine differences in more detail.

500

501 **Acknowledgements**

502 This work was supported by the National Science Foundation (AGS-1347491 and AGS-
503 1347499). Special thanks to Luke Allen, Sara Berry, Michael Tai Bryant, Nicole Corbin, Jason
504 Endries, Levi Lovell, Matthew Miller, Emma Scott, Laura Tomkins for their work with radar
505 data processing and analysis.

506

507

508 **References**

509 Baxter, M. and P. Schumacher, 2017: Distribution of single-banded snowfall in Central United
510 States cyclones. *Wea. Forecasting*, **32**, 533–554.

511 Bjerknes, J., and H. Solberg, 1922: Life cycle of cyclones and the polar front theory of
512 atmospheric circulation. *Geophys. Publ.*, **3**, 3–18.

513 Brown, B.G., R. Bullock, J. Halley Gotway, D. Ahijevych, C. Davis, E. Gilleland, and L.
514 Holland, 2007: Application of the MODE object-based verification tool for the evaluation
515 of model precipitation fields. *AMS 22nd Conference on Weather Analysis and*
516 *Forecasting and 18th Conference on Numerical Weather Prediction*, 25–29 June, Park
517 City, Utah, Amer. Meteor. Soc.

518 Bullock, R. G., B. G. Brown, and T. L. Fowler, 2016: Method for object-based diagnostic
519 evaluation. NCAR Tech. Note. NCAR/TN-532+STR, 84 pp, doi:10.5065/D61V5CBS.

520 Charles, M. E., and B. A. Colle, 2009: Verification of extratropical cyclones within the NCEP
521 operational models. Part I: analysis errors and short-term NAM and GFS forecasts. *Wea.*
522 *Forecasting*, **24**, 1173–1190.

523 Clark, J. H. E., R. P. James, and R. H. Grumm, 2002: A reexamination of the mechanisms
524 responsible for banded precipitation. *Mon. Wea. Rev.*, **130**, 3074–3086.

525 Colle, B. A., D. Stark, and S. E. Yuter, 2014: Surface microphysical observations within East
526 Coast winter storms on Long Island, NY. *Mon. Wea. Rev.*, **142**, 3126–3146.

527 Colle, B. A., Z. Zhang, K. A. Lombardo, E. Chang, P. Liu, and M. Zhang, 2013: Historical
528 evaluation and future prediction of Eastern North American and Western Atlantic
529 extratropical cyclones in the CMIP5 models during the cool season. *J. Climate*, **26**, 6882–
530 6903.

531 Corbin, N. A., 2016: Northern California’s Central Valley spatial precipitation patterns

532 associated with atmospheric rivers under different environmental conditions, M.S.
533 Thesis, Dept. of Marine, Earth, Atmospheric Sciences, North Carolina State University,
534 227 pp.

535 Davis, C.A., B.G. Brown, and R.G. Bullock, 2006a: Object-based verification of precipitation
536 forecasts, Part I: Methodology and application to mesoscale rain areas. *Mon. Wea. Rev.*,
537 **134**, 1772–1784.

538 Davis, C.A., B.G. Brown, and R.G. Bullock, 2006b: Object-based verification of precipitation
539 forecasts, Part II: Application to convective rain systems. *Mon. Wea. Rev.*, **134**, 1785–
540 1795.

541 Developmental Testbed Center, 2015: MET: Version 5.1 Model Evaluation Tools Users Guide.
542 317 pp. [Available online at <http://www.dtcenter.org/met/users/docs/overview.php>.]
543 Emanuel, K. A., 1985: Frontal circulations in the presence of small moist symmetric stability.
544 *J. Atmos. Sci.*, **42**, 1062–1071.

545 Fairman Jr, J. G., D. M. Schultz, D. J. Kirshbaum, S. L. Gray, and A. I. Barrett, 2016:
546 Climatology of banded precipitation over the contiguous united states. *Mon. Wea. Rev.*,
547 **144**, 4553–4568.

548 Ganetis, S., and B. Colle, 2015: The thermodynamic and microphysical evolution of an intense
549 snowband during the Northeast U.S. blizzard of 8-9 February 2013. *Mon Wea. Rev.*, **143**,
550 4104-4125.

551 Hoban, N. P., 2016: Observed characteristics of mesoscale banding in Coastal Northeast U.S.
552 snow storms, M.S. Thesis, Dept. of Marine, Earth, Atmospheric Sciences, North Carolina
553 State University, 66 pp.

554 Hodges, K. I., 1995: Feature tracking on the unit sphere. *Mon. Wea. Rev.*, **123**, 3458–3465.

555 Jurewicz, M. L., and M. S. Evans, 2004: A Comparison of two banded, heavy snowstorms
556 with very different synoptic settings. *Wea. Forecasting*, **19**, 1011–1028.

557 Kenyon, J. S., 2013: The motion of mesoscale snowbands in Northeast U.S. winter storms, M.S.
558 Thesis, Dept. of Atmos. and Environmental Sci., University at Albany, State University
559 of New York, 108 pp.

560 Kocin, P., L. W. Uccellini, J. Alpert, B. Ballish, D. Bright, R. Grumm, and G. Manikin, 2011:
561 The blizzard of 25-27 December 2010: Forecast assessment. NOAA/NCEP event review.
562 [Available online at [http://www.wpc.ncep.noaa.gov/winter_storm_summaries/
563 event_reviews/2010/December25_27_2010_Blizzard.pdf](http://www.wpc.ncep.noaa.gov/winter_storm_summaries/event_reviews/2010/December25_27_2010_Blizzard.pdf).]

564 Krekeler, J., 2013: Great Lakes to Northeast major winter storm. NOAA/NCEP/WPC event
565 review. [Available online at [http://www.wpc.ncep.noaa.gov/winter_storm_summaries/
566 event_reviews/2013/Great_Lakes_Northeast_Winter_Storm_Feb2013.pdf](http://www.wpc.ncep.noaa.gov/winter_storm_summaries/event_reviews/2013/Great_Lakes_Northeast_Winter_Storm_Feb2013.pdf).]

567 Lawson, J. R., and W. A. Gallus, 2016: Adapting the SAL method to evaluate reflectivity
568 forecasts of summer precipitation in the central United States. *Atmos. Sci. Lett.*, **17**, 524-
569 530.

570 McCann, D. W., 1995: Three-dimensional computations of equivalent potential vorticity. *Wea.*
571 *Forecasting*, **10**, 798–802.

572 Moore, J. T., C. E. Graves, S. Ng, and J. L. Smith, 2005: A process-oriented methodology
573 toward understanding the organization of an extensive mesoscale snowband: A diagnostic
574 case study of 4–5 December 1999. *Wea. Forecasting*, **20**, 35-50.

575 Nicosia, D. J., and R. H. Grumm, 1999: Mesoscale band formation in three major Northeastern
576 United States snowstorms. *Wea. Forecasting*, **14**, 346-368.

577 Novak, D. R., L. F. Bosart, D. Keyser, and J. S. Waldstreicher, 2004: An observational study of

578 cold season–banded precipitation in Northeast U.S. cyclones. *Wea. Forecasting*, **19**, 993–
579 1010.

580 Novak, D. R., and B. A. Colle, 2012: Diagnosing snowband predictability using a multimodel
581 ensemble system. *Wea. Forecasting*, **27**, 565–585.

582 Novak, D. R., B. A. Colle, and A. R. Aiyyer, 2010: Evolution of mesoscale precipitation band
583 environments within the comma head of Northeast U.S. cyclones. *Mon. Wea. Rev.*, **138**,
584 2354–2374.

585 Novak, D. R., B. A. Colle, and R. McTaggart-Cowan, 2009: The role of moist processes in the
586 formation and evolution of mesoscale snowbands within the comma head of Northeast
587 U.S. cyclones. *Mon. Wea. Rev.*, **137**, 2662–2686.

588 Novak, D. R., B. A. Colle, and S. E. Yuter, 2008: High-resolution observations and model
589 simulations of the life cycle of an intense mesoscale snowband over the Northeastern
590 United States. *Mon. Wea. Rev.*, **136**, 1433–1456.

591 Petterssen, S., 1936: Contribution to the theory of frontogenesis. *Geofys. Publ.*, **11**(6), 1–27.

592 Picca, J. C., D. M. Schultz, B. A. Colle, S. Ganetis, D. R. Novak, and M. Sienkiewicz, 2014: The
593 value of dual-polarization radar in diagnosing the complex microphysical evolution of an
594 intense snowband. *Bull. Amer. Meteor. Soc.*, **95**, 1825–1834.

595 Saha, S., and Coauthors, 2010: The NCEP climate forecast system reanalysis. *Bull. Amer.*
596 *Meteor. Soc.*, **91**, 1015–1057.

597 Saha, S., and Coauthors, 2014: The NCEP climate forecast system version 2. *J. Climate*, **27**,
598 2185–2208.

599 Sanders, F., and L. F. Bosart, 1985a: Mesoscale structure in the Megalopolitan snowstorm of 11–

600 12 February 1983. Part I: frontogenetical forcing and symmetric instability. *J. Atmos.*
601 *Sci.*, **42**, 1050–1061.

602 Sanders, F., and L. F. Bosart, 1985b: Mesoscale structure in the Megalopolitan snowstorm, 11–
603 12 February 1983. Part II: doppler radar study of the New England snowband. *J. Atmos.*
604 *Sci.*, **42**, 1398–1407.

605 Schultz, D. M., and P. N. Schumacher, 1999: The use and misuse of conditional symmetric
606 instability. *Mon. Wea. Rev.*, **127**, 2709–2732.

607 Schultz, D. M., and G. Vaughan, 2010: Occluded fronts and the occlusion process: A fresh
608 look at conventional wisdom. *Bull. Amer. Meteor. Soc.*, **92**, 443–466.

609 Shapiro, M. A., and D. Keyser, 1990: Fronts, jet streams and the tropopause. Extratropical
610 cyclones: The Erik Palmén memorial volume, C.W. Newton and E. O. Holopainen, Eds.,
611 *Amer. Meteor. Soc.*, pp. 167–191.

612 Shields, M. T., R. M. Rauber, and M. K. Ramamurthy, 1991: Dynamical forcing and mesoscale
613 organization of precipitation bands in a Midwest winter cyclonic storm. *Mon. Wea. Rev.*,
614 **119**, 936–964.

615 Soltow, M., 2011: December 25-27, 2010, Winter storm, Eastern United States.
616 NOAA/NCEP/WPC event review. [Available online at [http://www.wpc.ncep.noaa.gov/
617 winter_storm_summaries/event_reviews/2010/Eastern_US_WinterStorm_December_201
618 0.pdf.](http://www.wpc.ncep.noaa.gov/winter_storm_summaries/event_reviews/2010/Eastern_US_WinterStorm_December_2010.pdf)]

619 Thorpe, A. J., and K. A. Emanuel, 1985: Frontogenesis in the presence of small stability to
620 slantwise convection. *J. Atmos. Sci.*, **42**, 1809–1824.

621 Wilks, D.S., 2011: *Statistical methods in the atmospheric sciences*, 3rd Ed. International
622 Geophysics Series, Vol. 100, Academic Press, 704 pp.

623 Wolfsberg, D. G., K. A. Emanuel, and R. E. Passarelli, 1986: Band formation in a New England
624 winter storm. *Mon. Wea. Rev.*, **114**, 1552–1569.

625 Xu, Q., 1989: Extended Sawyer–Eliassen equation for frontal circulations in the presence of
626 small viscous moist symmetric stability. *J. Atmos. Sci.*, **46**, 2671–2683.

627 Xu, Q., 1992: Formation and evolution of frontal rainbands and geostrophic potential vorticity
628 anomalies. *J. Atmos. Sci.*, **49**, 629–648.

629

630 **Table and Figure Captions**

631 **Table 1.** Criteria used to objectively classify objects output from the MET MODE tool applied to
632 stitched regional composite reflectivity data.

633 **Table 2.** Case classification by band type, cyclone stage, and band motion for 6-hourly events
634 during banded cases.

635 **Figure 1.** Map showing locations of six upper-air sites (green circles) used for vertical profiles
636 through regional classification given by each box bounding ~150-km around the upper-
637 air site. Locations of regional NWS WSR-88D radar (red circles) and Automated Surface
638 Observing System (ASOS) sites (purple squares) are shown.

639 **Figure 2.** Sea level pressure (SLP) along each of the 108 cyclone tracks in the study with points
640 along the track colored by SLP with warmer colors indicating weaker cyclones and
641 cooler colors indicating stronger cyclones.

642 **Figure 3.** Examples of 2-km AGL stitched regional composite reflectivity and the resulting
643 classified objects from the MET MODE tool output for the four banding classifications
644 exhibited in Northeast U.S. winter storms, (a) a large, single band, (b) multi-bands, (c)
645 both single and multi-bands, and (d) non-banded.

646

647 **Figure 4.** Distance and angle from cyclone low pressure center for 193 events for (a) SINGLE
648 events for mature (filled circle) and developing (open circle) cyclones for parallel moving
649 bands (light green) and perpendicular moving bands (dark green), (b) MULTI events for
650 mature (asterisk) and developing (plus sign) cyclones for parallel moving bands (light
651 blue) and perpendicular moving bands (dark blue), (c) BOTH events for mature (asterisk)
652 and developing (cross) cyclones for parallel moving bands (light purple) and
653 perpendicular moving bands (dark purple), (d) NONE events for mature (filled diamond)
654 and developing (open diamond) cyclones. The radial distance is in kilometers and the
655 angle from the cyclone to the sounding location at the center of the domain of the
656 classified event is in degrees.

657 **Figure 5.** Large band locations and orientations relative to the cyclone center (origin of plot)
658 with the radius in km and angle in degrees. Bands associated with mature cyclones are in
659 blue and developing cyclones are in red.

660 **Figure 6.** Vertical profiles of (a–e) temperature ($^{\circ}\text{C}$) and (f–j) relative humidity (%) for events
661 classified as (a,f) SINGLE in green, (b,g) MULTI in blue, (c,h) BOTH in purple, (d,i)
662 NONE. Red profiles in (a–d) indicate those that exhibit a stable 50-hPa layer ($dT/dP \geq$
663 $0.05^{\circ}\text{C hPa}^{-1}$). (e,j) Bold lines denote the average profile for each classification with
664 markers indicating 2.5th and 97.5th percentiles of the mean with 95% confidence.

665 **Figure 7.** As in Figure 6 but for (a–e) saturation equivalent potential temperature (K) and (f–j)
666 wind speed (kts). Red profiles in (a–d) indicate those that exhibit a conditionally unstable
667 50-hPa layer ($d\theta_e^*/dP \leq 0.02 \text{ K hPa}^{-1}$).

668 **Figure 8.** As in Figure 6 but for (a–e) frontogenesis ($\text{K } 100 \text{ km}^{-1} \text{ h}^{-1}$) and (f–j) saturation
669 equivalent potential vorticity (MPV*, PVU).

670

671 **Figure 9.** The relationship between 700–600-hPa averaged saturation equivalent potential

672 vorticity (MPV*, PVU) on the abscissa and 700-hPa frontogenesis ($K\ 100\ km^{-1}\ h^{-1}$) on

673 the ordinate for (a) SINGLE, (b) MULTI, (c) MULTI, (d) NONE classified events from

674 developing (DEV) or mature (MAT) cyclones exhibiting perpendicular (PERP) or

675 parallel (PARA) band motion.

676 **Figure 10.** Distribution of 800-700-hPa average frontogenesis for all 193 events in the dataset

677 colored by classification as either BOTH (magenta), SINGLE (green), MULTI (blue) or

678 NONE (gray).

679

680 **Tables & Figures**

681

682 **Table 1.** Criteria used to objectively classify objects output from the MET MODE tool applied to
683 stitched regional composite reflectivity data.
684

	Length (L)	Width (W)	Aspect Ratio (W/L)
Large Band	≥ 200 km	$20 \leq W \leq 100$ km	≤ 0.5
Mid-sized Band	< 200 km	$10 \leq W \leq 50$ km	≤ 0.5
Undefined/Cell	$10 \leq L \leq 100$ km	$10 \leq W \leq 100$ km	> 0.5

685

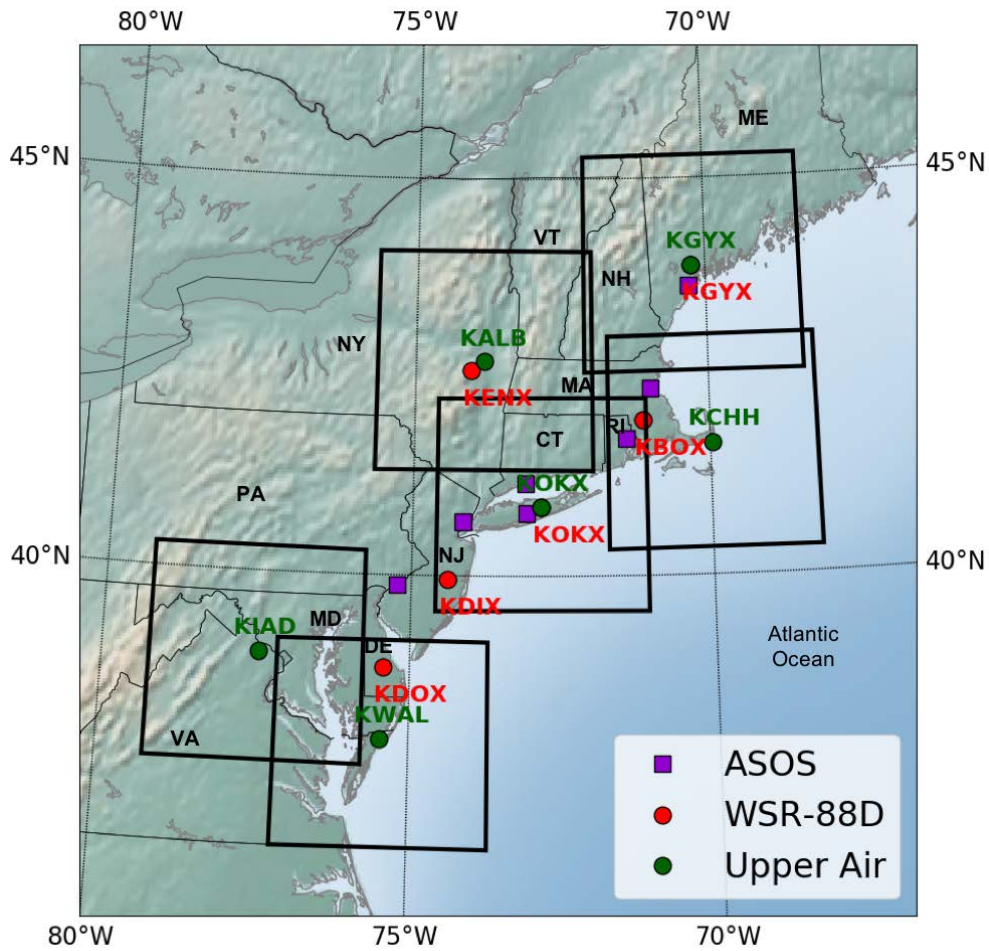
686

687
688
689

Table 2. Case classification by band type, cyclone stage, and band motion for 6-hourly events during banded cases.

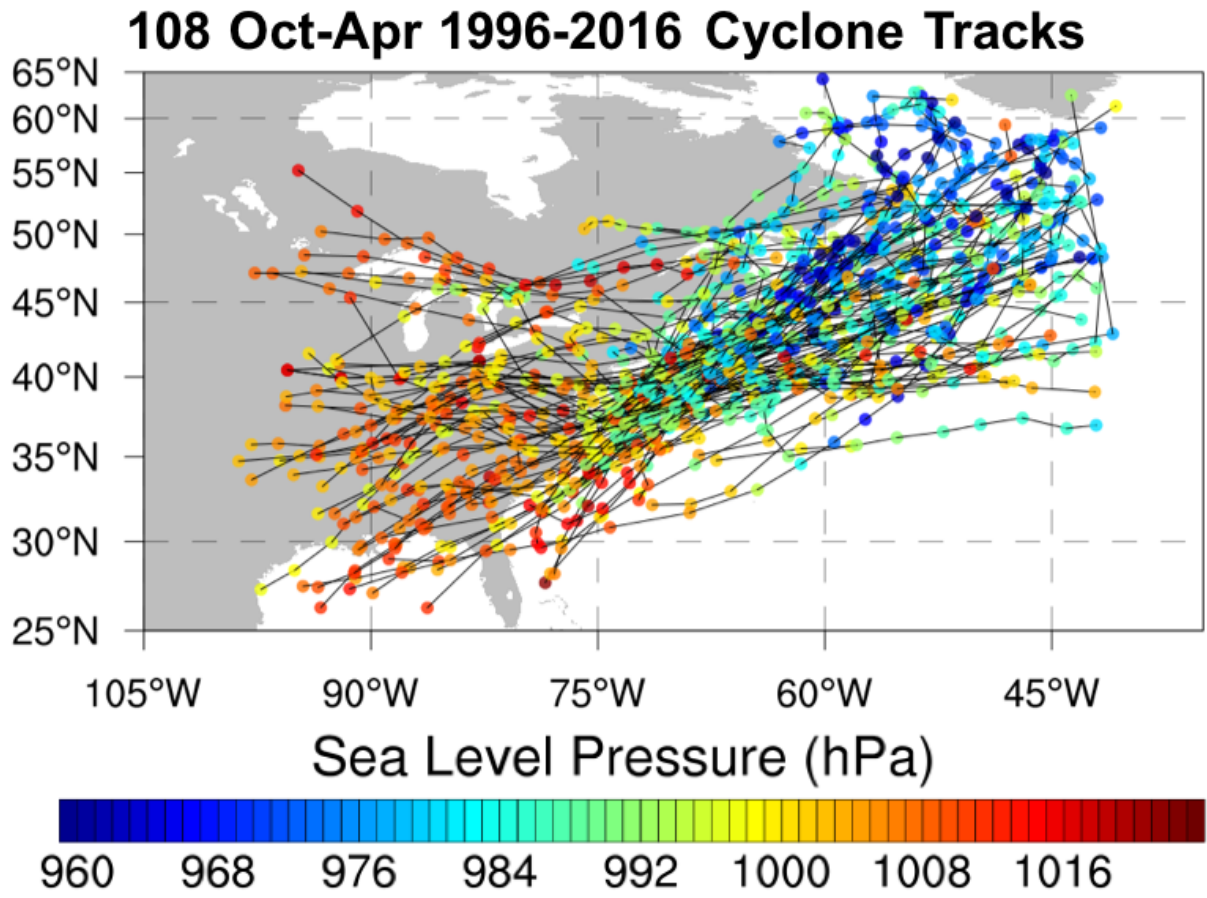
Classification	Cyclone Stage	Number of Events with Band Movement Perpendicular (Parallel) to the Long Axis of the Band
Single Band Only	Developing	0 (0)
	Mature	3 (2)
Multi-bands Only	Developing	6 (12)
	Mature	14 (3)
Both Single & Multi-bands	Developing	15 (28)
	Mature	58 (6)
Non-banded	Developing	29
	Mature	17

690
691
692
693



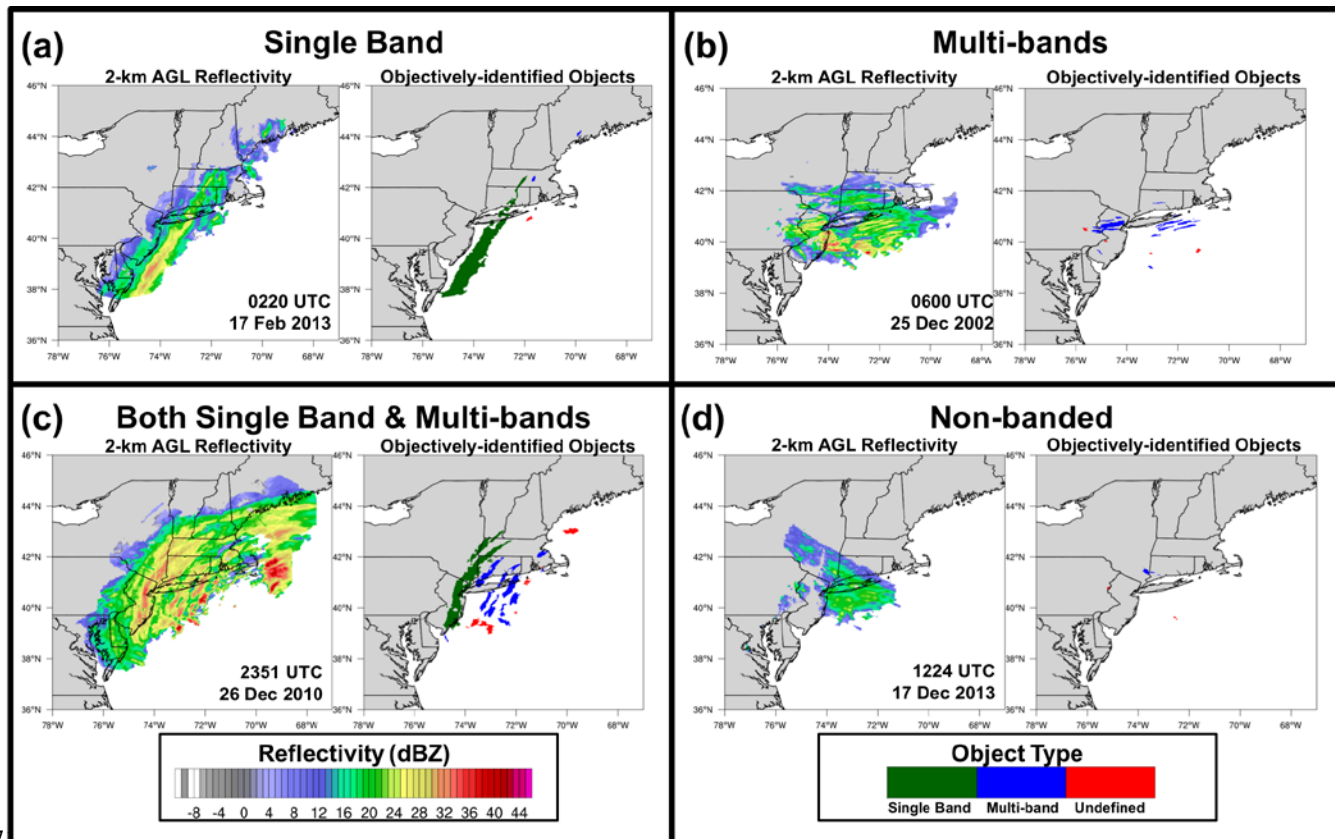
694
 695
 696
 697
 698
 699
 700

Figure 1. Map showing locations of six upper-air sites (green circles) used for vertical profiles through regional classification given by each box bounding ~150-km around the upper-air site. Locations of regional NWS WSR-88D radar (red circles) and Automated Surface Observing System (ASOS) sites (purple squares) are shown.



701
 702
 703
 704
 705
 706
 707
 708
 709
 710

Figure 2. Sea level pressure (SLP) along each of the 108 cyclone tracks in the study with points along the track colored by SLP with warmer colors indicating weaker cyclones and cooler colors indicating stronger cyclones.

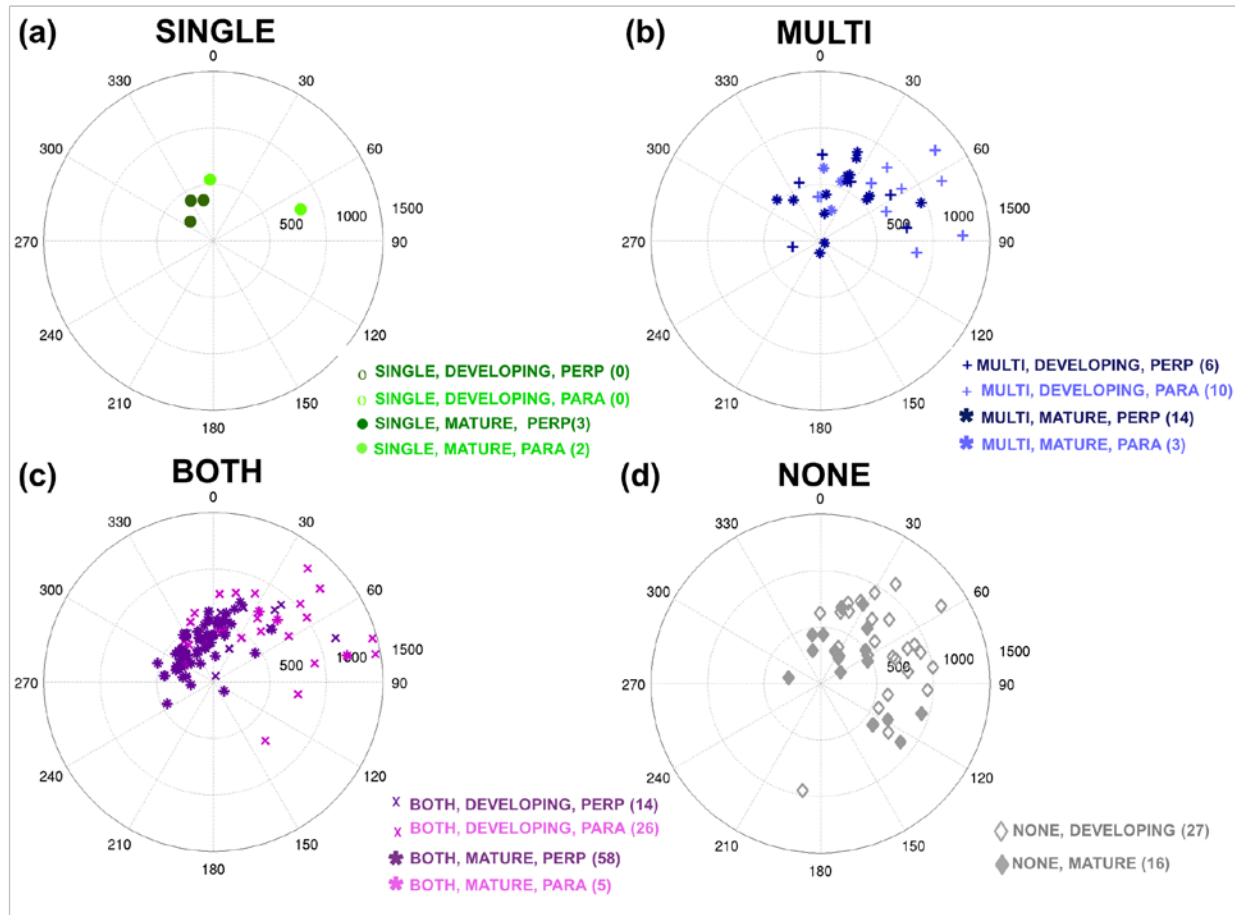


712

713 **Figure 3.** Examples of 2-km AGL stitched regional composite reflectivity and the resulting
 714 classified objects from the MET MODE tool output for the four banding classifications exhibited
 715 in Northeast U.S. winter storms, (a) a large, single band, (b) multi-bands, (c) both single and
 716 multi-bands, and (d) non-banded.

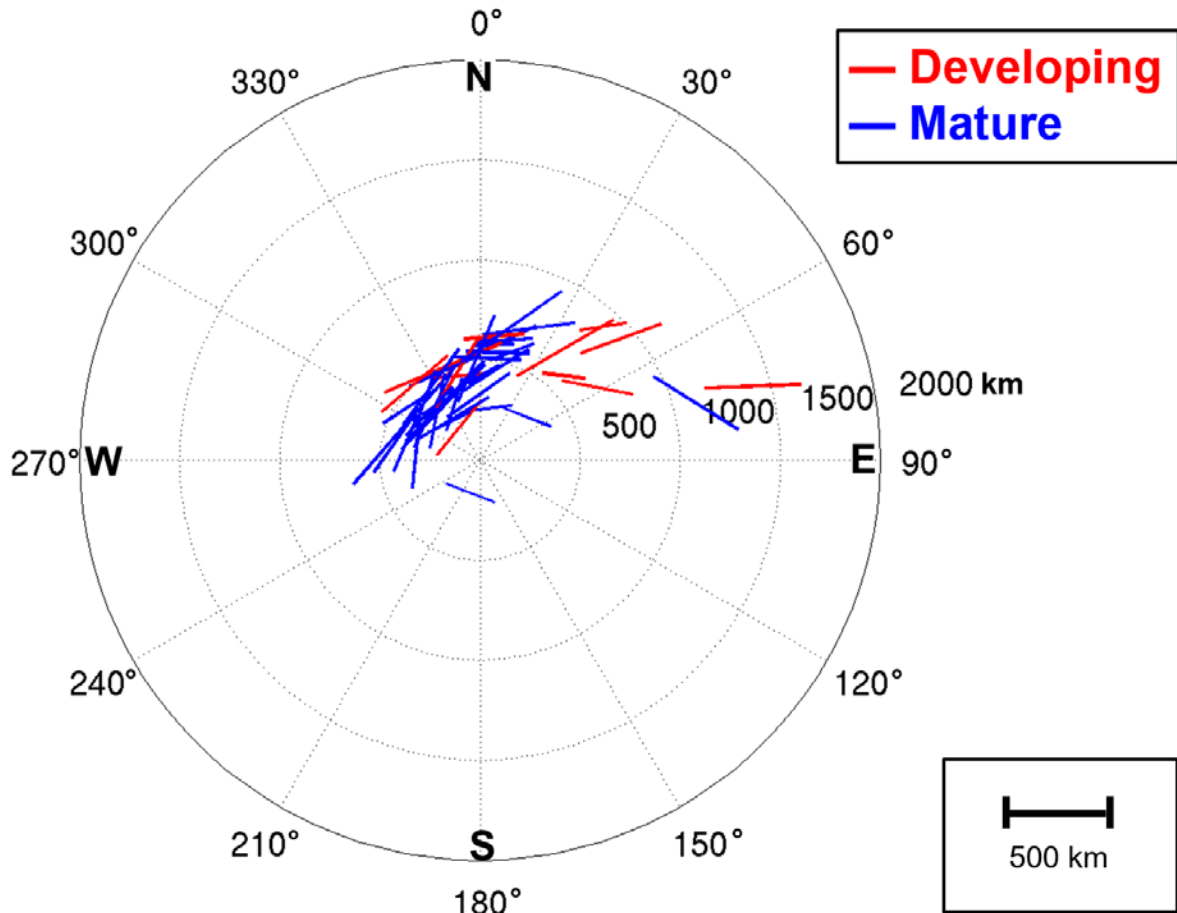
717

718



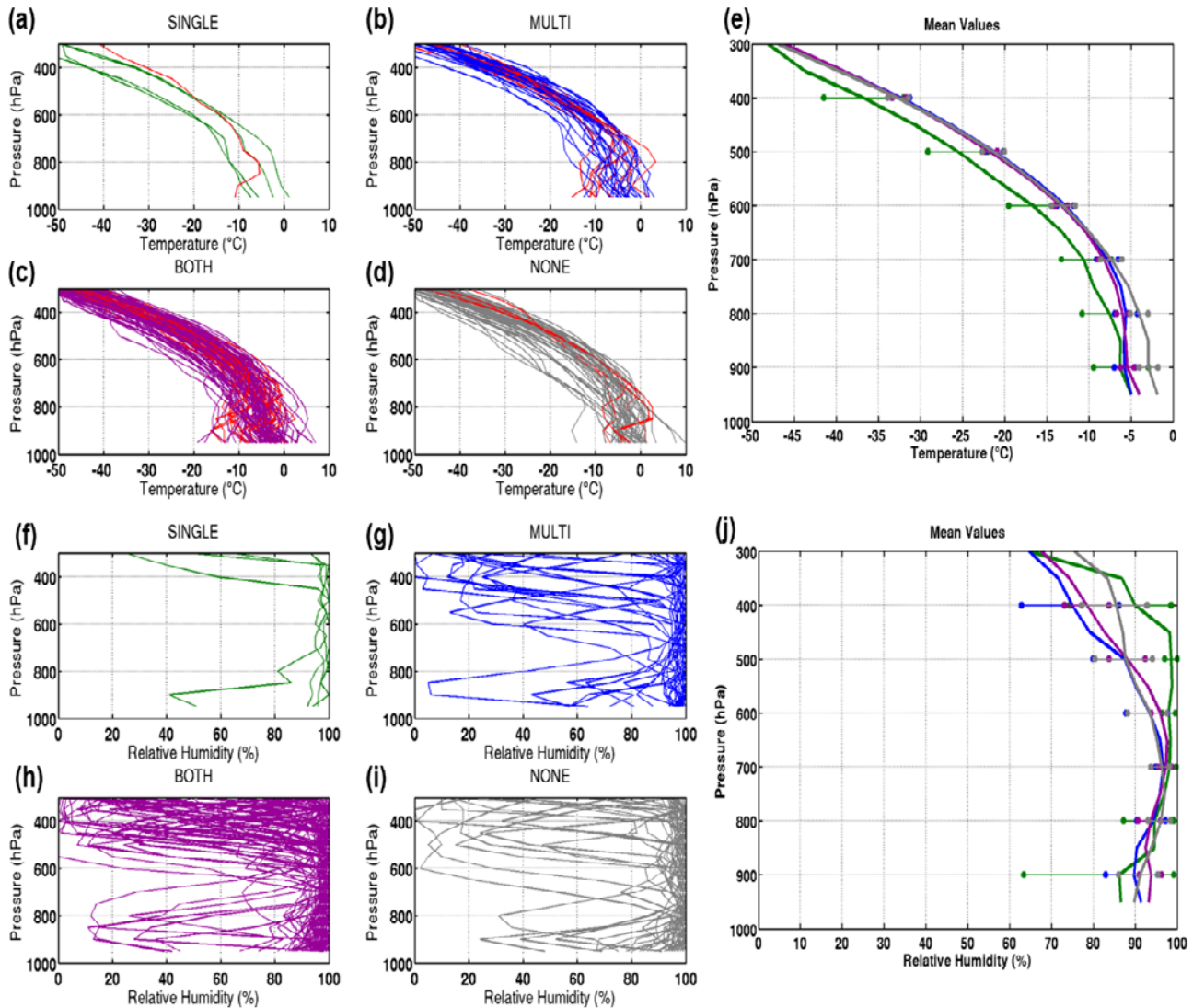
720
 721
 722
 723
 724
 725
 726
 727
 728
 729
 730
 731
 732

Figure 4. Distance and angle from cyclone low pressure center for 193 events for (a) SINGLE events for mature (filled circle) and developing (open circle) cyclones for parallel moving bands (light green) and perpendicular moving bands (dark green), (b) MULTI events for mature (asterisk) and developing (plus sign) cyclones for parallel moving bands (light blue) and perpendicular moving bands (dark blue), (c) BOTH events for mature (asterisk) and developing (cross) cyclones for parallel moving bands (light purple) and perpendicular moving bands (dark purple), (d) NONE events for mature (filled diamond) and developing (open diamond) cyclones. The radial distance is in kilometers and the angle from the cyclone to the sounding location at the center of the domain of the classified event is in degrees.



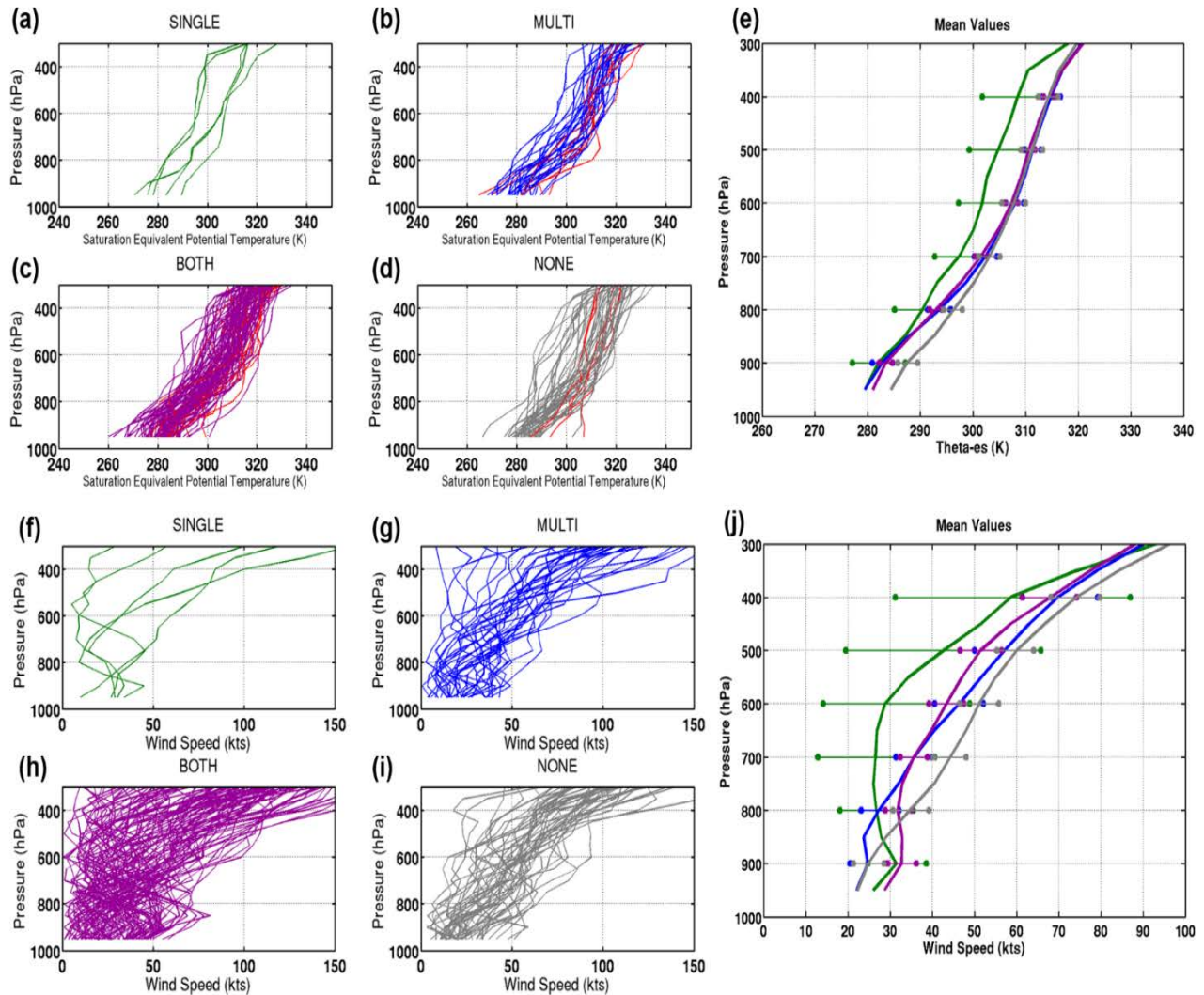
733
 734
 735
 736
 737
 738
 739

Figure 5. Large band locations and orientations relative to the cyclone center (origin of plot) with the radius in km and angle in degrees. Bands associated with mature cyclones are in blue and developing cyclones are in red.



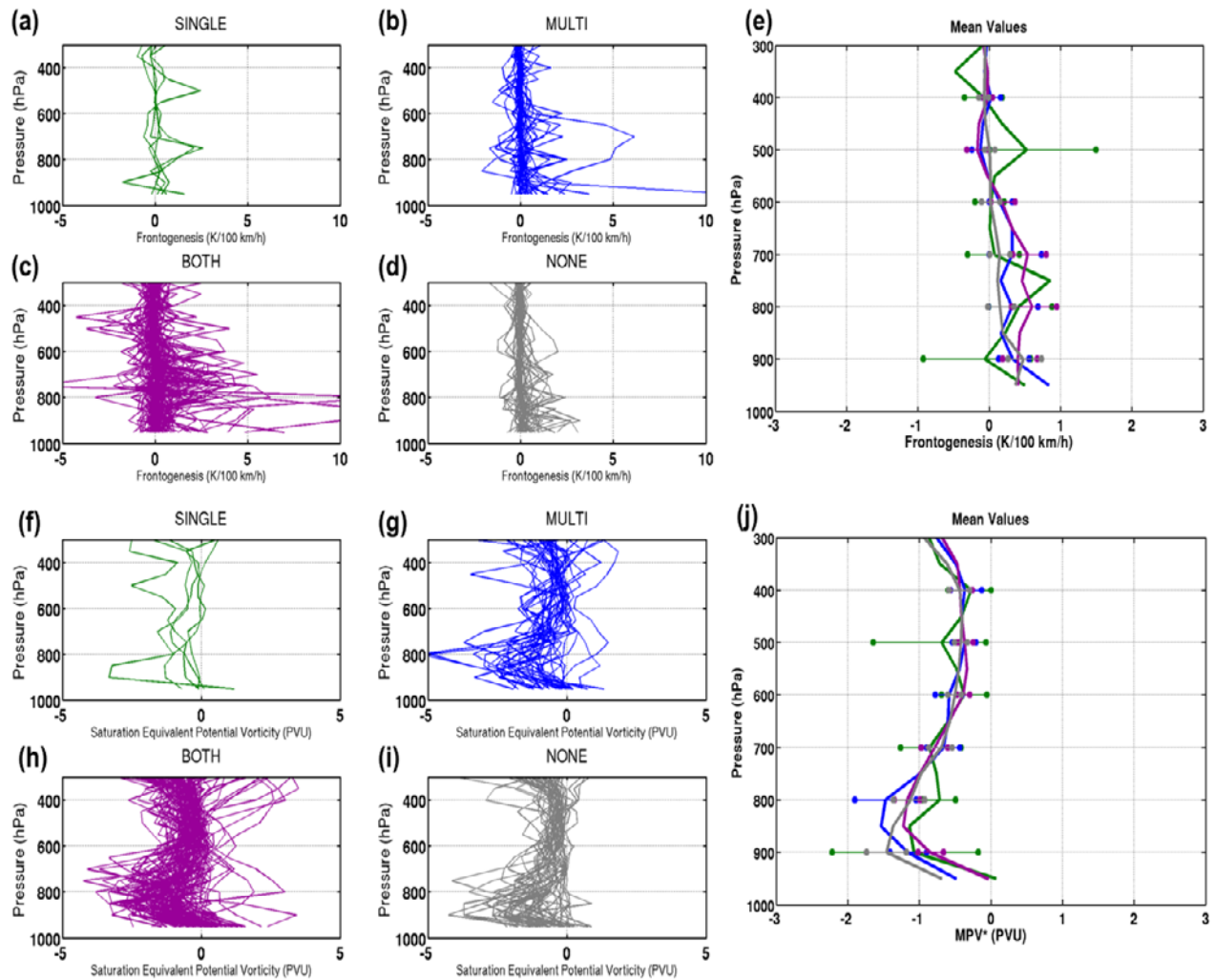
740
 741
 742 **Figure 6.** Vertical profiles of (a–e) temperature (°C) and (f–j) relative humidity (%) for events
 743 classified as (a,f) SINGLE in green, (b,g) MULTI in blue, (c,h) BOTH in purple, (d,i) NONE.
 744 Red profiles in (a-d) indicate those that exhibit a stable 50-hPa layer ($dT/dP \geq 0.05^\circ\text{C hPa}^{-1}$). (e,j)
 745 Bold lines denote the average profile for each classification with markers indicating 2.5th and
 746 97.5th percentiles of the mean with 95% confidence.
 747

748



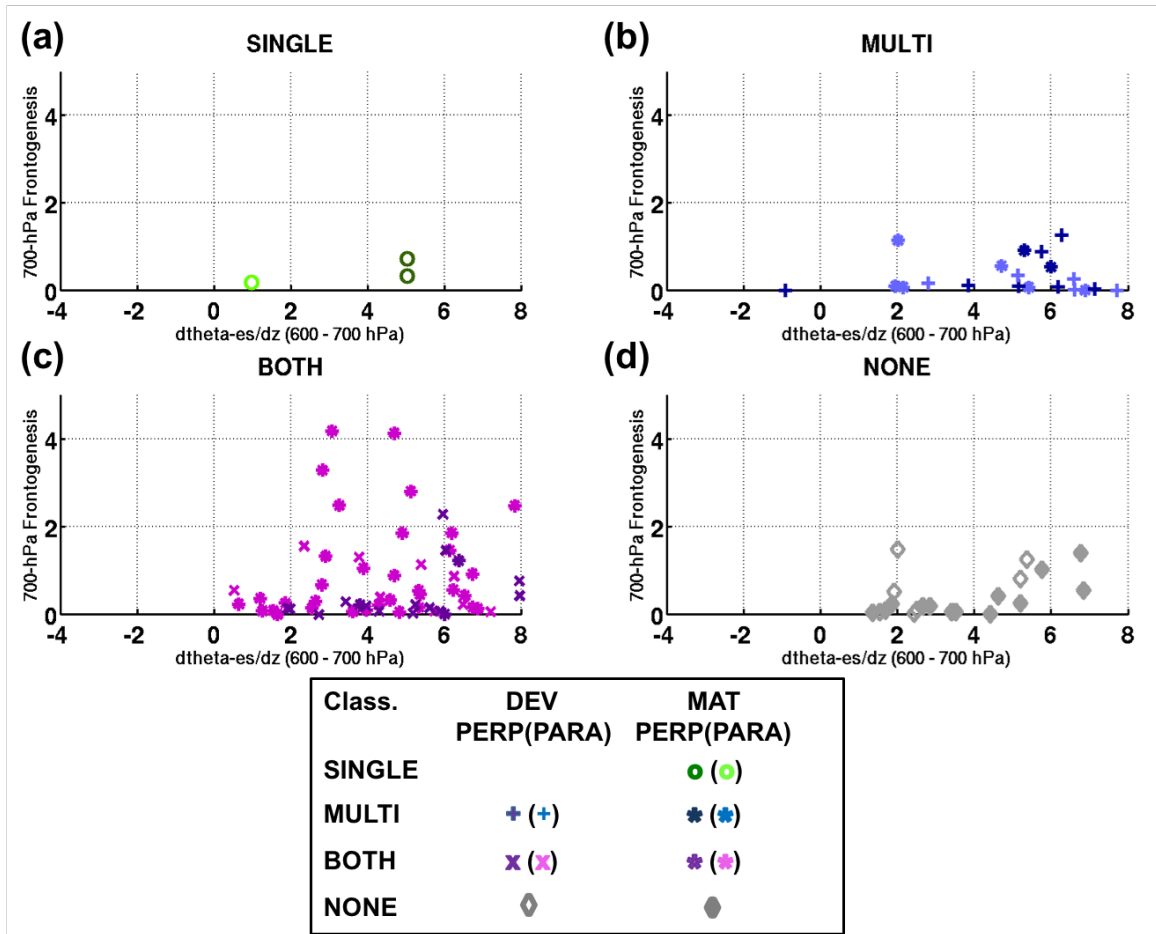
749
 750
 751
 752
 753
 754
 755

Figure 7. As in Figure 6 but for (a–e) saturation equivalent potential temperature (K) and (f–j) wind speed (kts). Red profiles in (a–d) indicate those that exhibit a conditionally unstable 50-hPa layer ($d\theta_e^*/dP \leq 0.02 \text{ K hPa}^{-1}$).



757
 758
 759
 760
 761
 762
 763

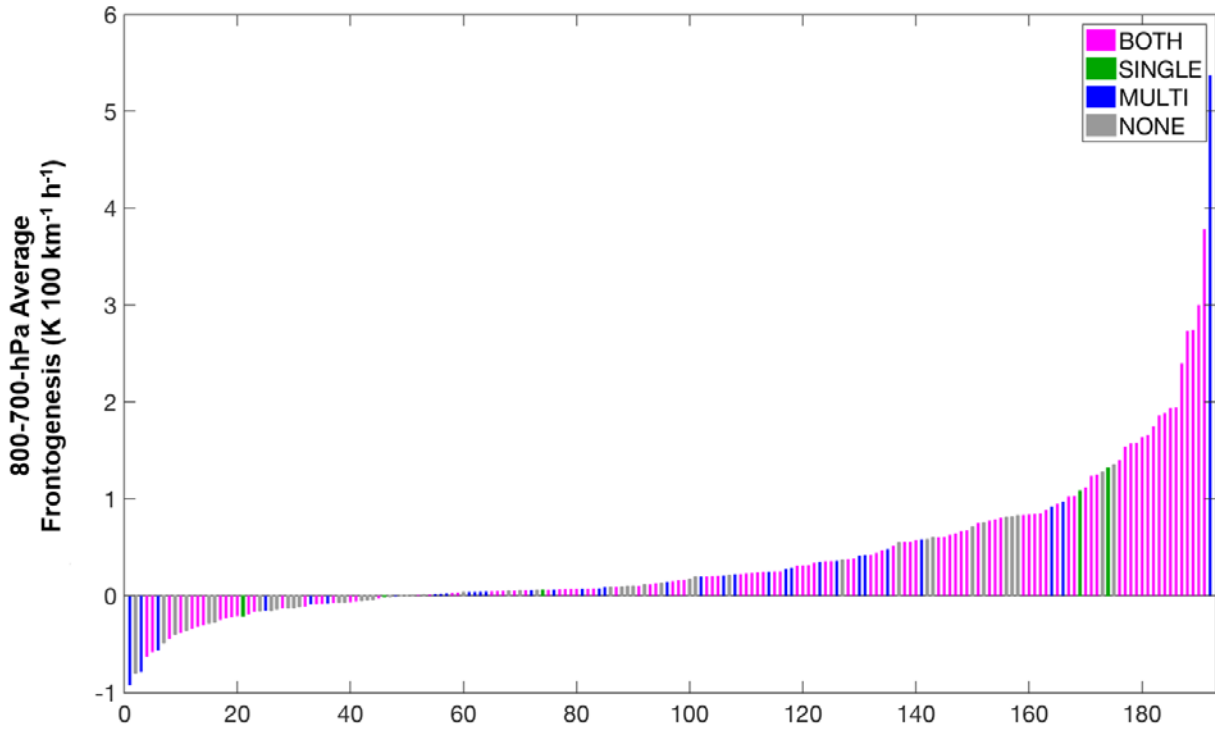
Figure 8. As in Figure 6 but for (a–e) frontogenesis ($\text{K } 100 \text{ km}^{-1} \text{ h}^{-1}$) and (f–j) saturation equivalent potential vorticity (MPV*, PVU).



764
 765
 766
 767
 768
 769
 770
 771
 772

Figure 9. The relationship between 700–600-hPa averaged saturation equivalent potential vorticity (MPV*, PVU) on the abscissa and 700-hPa frontogenesis ($K\ 100\ km^{-1}\ h^{-1}$) on the ordinate for (a) SINGLE, (b) MULTI, (c) MULTI, (d) NONE classified events from developing (DEV) or mature (MAT) cyclones exhibiting perpendicular (PERP) or parallel (PARA) band motion.

Distribution of 800-700-hPa averaged frontogenesis



773
774 **Figure 10.** Distribution of 800-700-hPa average frontogenesis for all 193 events in the dataset
775 colored by classification as either BOTH (magenta), SINGLE (green), MULTI (blue) or NONE
776 (gray).

777
778
779
780
781
782
783
784
785
786
787